

Nonmonotonically tunable Rashba spin-orbit coupling by multiple-band filling control in SrTiO₃-based interfacial *d*-electron gases

Haixing Liang,¹ Long Cheng,¹ Laiming Wei,^{1,*} Zhenlin Luo,² Guolin Yu,³ Changgan Zeng,^{1,4,5,†} and Zhenyu Zhang^{4,5}¹Hefei National Laboratory for Physical Sciences at the Microscale (HFNL), CAS Key Laboratory of Strongly Coupled Quantum Matter Physics, and Department of Physics, University of Science and Technology of China, Hefei, Anhui 230026, China²National Synchrotron Radiation Laboratory, University of Science and Technology of China, Hefei, Anhui 230026, China³National Laboratory for Infrared Physics, Shanghai Institute of Technical Physics, Chinese Academy of Science, Shanghai 200083, China⁴International Center for Quantum Design of Functional Materials (ICQD), HFNL, University of Science and Technology of China, Hefei, Anhui 230026, China⁵Synergetic Innovation Center of Quantum Information and Quantum Physics, University of Science and Technology of China, Hefei, Anhui 230026, China

(Received 30 January 2015; revised manuscript received 19 May 2015; published 12 August 2015)

Spin-orbit coupling (SOC) for *d*-electron gas can be substantially enriched compared with the *sp*-electron gas due to the delicate ordering of the multiple *d* subbands. Here, we demonstrate the nontrivial Rashba SOC effect at SrTiO₃-based interfaces (LaAlO₃/SrTiO₃ and LaVO₃/SrTiO₃) directly related to the Ti 3*d* subband ordering via magnetotransport characterizations. Unusual *k*-cubic Rashba SOC contributed from the *d*_{xz/yz} states is revealed. More strikingly, when a gate voltage is swept to tune the band filling, the SOC strength initially increases and then decreases to form a dome feature, accompanied by an apparent single- to two-carrier transition. These two concomitant effects strongly indicate that the SOC behavior is largely determined by the Ti 3*d* subbands regardless of the overlayer boundary conditions, with the SOC strength peaked at the *d*_{xy}-*d*_{xz/yz} crossings due to the band hybridization effect as predicted. The present findings offer new insights into exploration of oxide-based quantum phases and spintronic devices.

DOI: [10.1103/PhysRevB.92.075309](https://doi.org/10.1103/PhysRevB.92.075309)

PACS number(s): 72.15.Rn, 73.40.-c, 75.70.Tj

I. INTRODUCTION

The Rashba spin-orbit coupling (SOC) at interfaces, a consequence of structure inversion asymmetry, is a key ingredient in spintronics [1,2]. At conventional semiconductor interfaces where the conductivity is dominated by *sp* electrons, usually only one *sp*-derived subband is occupied for typical carrier densities [3], and the SOC strength is largely determined by the interfacial electric fields, consistent with a simple Rashba picture [4–6]. However, when the interfacial electrons move in *d* bands, the strongly anisotropic nature of the *d* orbitals and the quantum confinement synergetically result in delicate ordering of the *d* subbands [7], and the inter-*d*-subband interactions may develop complicated spin-orbit textures [8], thus giving rise to much richer SOC behaviors than the counterpart of an *sp*-electron gas as proposed theoretically [8–12]. In particular, significant SOC enhancement has been theoretically predicted at the *d*_{xy}-*d*_{xz/yz} crossings due to the strong orbital hybridization [8–12]. This predicted behavior may enhance the SOC tunability by delicately manipulating the *d* multiband structure and band filling for future spintronic applications.

An archetypical two-dimensional (2D) *d*-electron system is formed at the interface between polar LaAlO₃ and nonpolar SrTiO₃ (LAO/STO) [13]. Extensive earlier studies have pointed to the identification that the electrons spatially confined at the interfaces and accounting for the interfacial conductivity are those residing in the multiple subbands originally derived from the Ti 3*d* orbitals [9–12,14–22]. Aside from LAO/STO, the interfaces of the nonpolar STO in proximity to

other polar band insulators (e.g., LaGaO₃ [23]) or even polar Mott insulators (e.g., LaVO₃ (LVO) [24]) have been revealed to be conducting as well. These STO-based 2D systems offer a unique platform for exploring the characteristics of *d*-electron SOC. Previous studies did uncover tunability in the SOC at the LAO/STO interface and STO surface [25–27], but the reported findings were controversial, with increasing [26,27] or decreasing [25] spin-orbit splitting upon increasing the gate voltage (*V*_g). A direct and complete correlation between the tunability of the SOC strength and intrinsic *d* subband structures remains to be unambiguously established.

In this paper, we demonstrate a definitive verification of an unconventional SOC effect related to the delicate Ti 3*d* subbands via weak antilocalization (WAL) and Hall characterizations, using the LAO/STO and LVO/STO as two prototype systems. In response to the sweeping *V*_g, the strength of the dominant *k*-cubic SOC mainly contributed from the *d*_{xz/yz} states first increases and then decreases to form a dome feature, accompanied by an apparent single- to two-carrier transition. These commonality observations suggest that the SOC behavior can be mainly attributed to the Ti 3*d* subband ordering irrespective of the detailed boundary conditions defined by the overlayer materials, and the spin splitting maximum emerges at the *d*_{xy}-*d*_{xz/yz} crossing region, where the SOC is enhanced due to the orbital mixing.

II. EXPERIMENT

High-quality LAO and LVO overlayers were grown on STO (001) substrates with atomic-layer control as described in Ref. [18]. Undoped STO(001) single crystals (CrysTec) were etched using an NH₄F-buffered HF solution after ultrasonic

*Corresponding author: laiming@ustc.edu.cn†Corresponding author: cgzeng@ustc.edu.cn

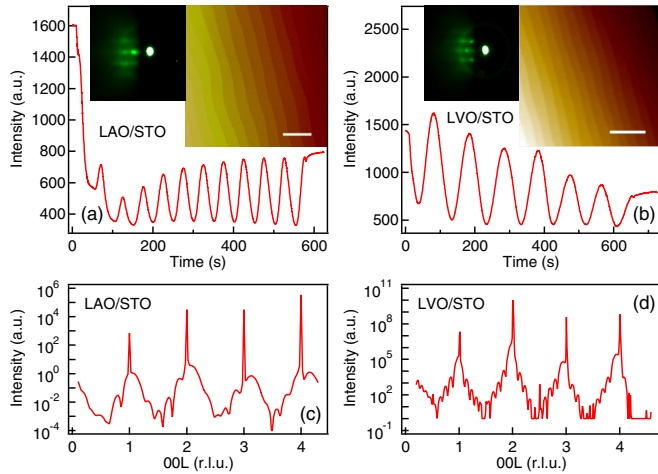


FIG. 1. (Color online) (a), (b) RHEED oscillations for the LAO (LVO) overlayers grown on STO substrates. The insets show the corresponding RHEED patterns and AFM images after growth. The scale bars in the AFM images are $1 \mu\text{m}$ and $0.5 \mu\text{m}$ for the LAO/STO and LVO/STO, respectively. (c), (d) X-ray diffraction patterns along the 00L crystal truncation rod for the 5-uc LAO/STO and 10-uc LVO/STO, respectively.

rinsing in deionized water. The crystals were subsequently annealed at 1000°C in an oxygen atmosphere to obtain an atomically flat surface with TiO_2 termination. Next, LAO (LVO) layers were grown on the treated STO substrates using pulsed laser deposition at 670°C (630°C) with an oxygen pressure of 1×10^{-4} mbar (2×10^{-6} mbar) and a KrF laser. The LAO (LVO) thickness was monitored *in situ* by reflection high-energy electron diffraction (RHEED) intensity oscillations, as depicted in Figs. 1(a) and 1(b). After growth, the samples were cooled to room temperature at the same growth oxygen pressure. The atomic terraces in the atomic force microscopy (AFM) image [insets of Figs. 1(a) and 1(b)] confirm the flatness of the LAO (LVO) surface. The superior quality of the LAO/STO (LVO/STO) heterostructures was further revealed by high-resolution x-ray diffraction along the 00L crystal truncation rod [see Figs. 1(c) and 1(d)]. Synchrotron x-ray measurements of the LAO/STO and LVO/STO samples were conducted at the Advanced Photon Source.

Standard Hall bars were mechanically patterned on the LAO/STO and LVO/STO samples, and Al wires were connected to the interfaces using ultrasonic welding. A back-gate Au electrode was deposited on the STO bottom with STO serving as the dielectric layer. The thicknesses of the LAO and LVO overlayers are both 11 unit cells (uc) for the transport measurements, which were performed in an Oxford Instruments ^4He cryostat at 1.5 K unless otherwise specified. The magnetic field was applied perpendicular to the sample plane. Standard low-frequency ac lock-in techniques were used to measure the longitudinal and Hall resistivity. An electrometer (Keithley 6514) was connected to the interfaces in series to measure the V_g -dependent electron densities. Before that, we measured successfully a standard capacitor adopting the same method. The V_g was initially ramped to the highest accessible positive value (210 V) to achieve reversible and reproducible V_g -dependent transport characteristics [29].

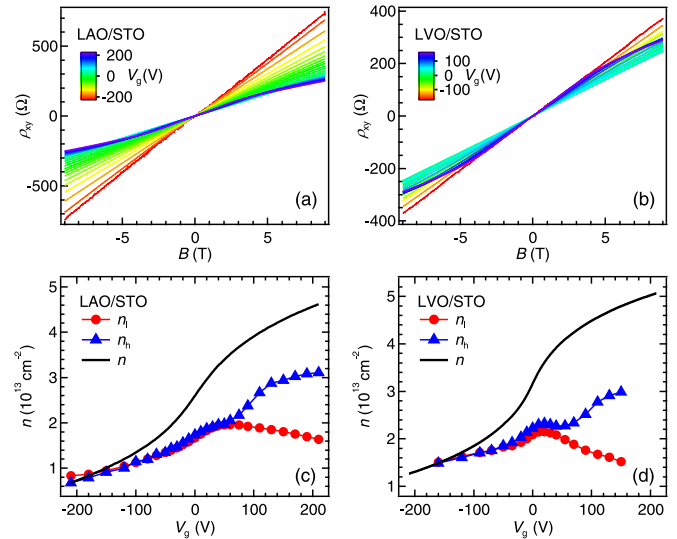


FIG. 2. (Color online) (a), (b) The ρ_{xy} as a function of B at various V_g s for the LAO/STO and LVO/STO, respectively. (c), (d) The n_l , n_h , and n as functions of V_g for the LAO/STO and LVO/STO, respectively. The thicknesses of the LAO and LVO adopted for the measurements are 11 uc.

III. RESULTS AND DISCUSSION

A. Hall analysis

Figures 2(a) and 2(b) display the Hall resistivity (ρ_{xy}) dependent on the magnetic field (B) at various V_g s. For both interfaces, a transition from linear to kinked is observed in the ρ_{xy} - B curves when V_g is increased. The critical V_g is about 30 V and 20 V for the LAO/STO and LVO/STO, respectively (corresponding total electron density of $3.1 \times 10^{13} \text{ cm}^{-2}$ and $3.6 \times 10^{13} \text{ cm}^{-2}$, respectively). Such linear-to-kinked transition has been reported previously [12]. According to the theoretical studies [8–12], the light d_{xy} subband locates at the bottom followed by the heavy $d_{xz/yz}$ subbands [see Fig. 5(b)] due to the quantum confinement [7]. The observed linear-to-kinked transition in the ρ_{xy} - B curves for both the LAO/STO and LVO/STO suggests ordering of the Ti $3d$ subbands, and can be attributed to an apparent transition from one- (d_{xy}) to two-carrier (d_{xy} and $d_{xz/yz}$) transport (this picture is not accurate as will be discussed later in Sec. III C) [12].

Following the route adopted in Ref. [12], we extracted the electron densities n_l and n_h from the Hall coefficients near 0 T and 9 T, which roughly reflect the electron density with higher mobility and the total electron density, respectively. As shown in Figs. 2(c) and 2(d), n_h and n_l are nearly identical initially, and deviate from each other when V_g passes a critical value [12]. The n_h roughly rises with increasing V_g as expected. However, both n_h and n_l may decrease at some certain V_g ranges, which is probably caused by the fact that the largest accessible magnetic field is only 9 T, not large enough to make n_h reflect the accurate total carrier densities [28]. In order to obtain more accurate total electron density, we performed charge measurement as a function of V_g [28,29], and the results are shown in Figs. 2(c) and 2(d). It is clear that the total electron density (denoted as n thereafter) increases

monotonically with increasing V_g . The rapid variation of the $n(V_g)$ curve near $V_g = 0$ V has also been observed previously for the LAO/STO [29] and LaTiO₃/STO [28], and could be attributed to the characteristic of the dielectric constant of the STO substrate. We choose the n_h estimated from the Hall data for the lowest V_g as the absolute value to calibrate n following previous study [28].

B. WAL analysis

The revealed effective tuning of Ti 3d band filling may lead to nontrivial SOC effects. The measured relative conductivities ($\Delta\sigma$) as functions of B at various V_g s are shown in Figs. 3(a) and 3(b), respectively. Similar behaviors are revealed for both the LAO/STO and LVO/STO interfaces: At large negative V_g s, only positive magnetoconductivity is observed, which can be primarily attributed to weak localization (WL) [30]; as V_g increases, negative magnetoconductivity starts to emerge around zero field to form a peak superimposed on the positive WL magnetoconductivity background, which is a signature of WAL [30]. The magnetic field where the magnetoconductivity dip locates is denoted as B_{\min} .

Next we further validate the WL/WAL attribution in three points. First, in principle, the WL/WAL corrections can be significant even when the magnetic field is extended to several teslas if the mean-free path is short enough. In the WL/WAL framework, the coherent backscattering takes place when $L_{tr} < L_i$ ($L_{tr} = \hbar\sqrt{2\pi n}/\mu$ is the mean-free path, μ is the Hall mobility, and L_i is the phase coherence length), resulting in the quantum corrections to the classical conductivity. An applied magnetic field B may suppress the coherent backscattering; however such WL/WAL corrections could still survive at high magnetic fields if L_{tr} is short enough, e.g., $L_B > L_{tr}$ ($L_B = \sqrt{\hbar/(eB)}$ is the magnetic length) [31]. These inequalities are indeed confirmed by the estimated parameters from the transport results. For the LAO/STO sample at $V_g = 0$ V, L_{tr} is determined to be 7.86 nm. For a field of 9 T, $L_B = 8.55$ nm, still larger than L_{tr} . As a cross-check, the WAL fit (details will be discussed later) yields $L_i = 58.7$ nm, satisfying $L_{tr} < L_i$. Similar results have also been found for the LVO/STO sample.

Second, a simple two-carrier model [32,33] fails to explain the magnetoresistivities [$\rho_{xx}(B)$] of the LAO/STO and LVO/STO systems both qualitatively and quantitatively. Qualitatively, as shown in Fig. 3(c), the fittings adopting the two-carrier model deviate substantially from the experimental data, especially at high fields. In addition, the parameters obtained from the fittings are quantitatively unreasonable. For example, the total density given by such two-carrier fittings would be $\sim 10^{11}$ cm⁻² for the LAO/STO (LVO/STO) at $V_g = 0$ V, which is two orders of magnitude lower than that ($\sim 10^{13}$ cm⁻²) obtained more reliably from the Hall and charge measurements.

Third and more importantly, we have performed magnetotransport measurements for another LVO/STO sample at different temperatures. The results are shown in Fig. 3(d). Indeed, as the temperature increases, both the negative magnetoconductivity at low fields and positive magnetoconductivity at high fields quickly vanish, as expected within the WAL/WL picture due to the quickly decreasing phase coherence length at increasing temperatures [30]. Therefore the WL/WAL

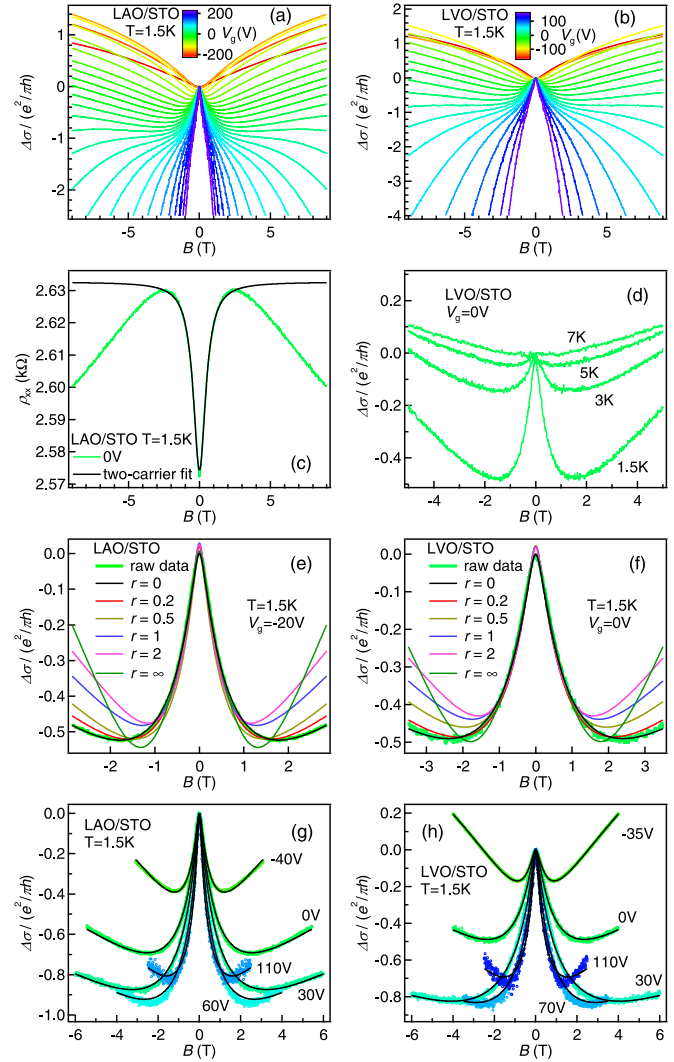


FIG. 3. (Color online) (a), (b) The relative conductivity $\Delta\sigma = \sigma(B) - \sigma(0)$ in units of $e^2/\pi h$ (e is the unit charge and h the Planck constant) as a function of B at various V_g s for the LAO/STO and LVO/STO, respectively. (c) The magnetoresistivity ρ_{xx} with fittings adopting the two-carrier model for the LAO/STO at $V_g = 0$ V. (d) $\Delta\sigma$ for another LVO/STO sample at various temperatures. (e), (f) $\Delta\sigma$ and the fitting curves by adopting the ILP model at various $r = B_{s01}/B_{s03}$ for the LAO/STO ($V_g = -20$ V) and LVO/STO ($V_g = 0$ V), respectively. (g), (h) $\Delta\sigma$ with the B^2 magnetoresistivity background subtracted at various V_g s and the fitting curves with only the k -cubic term taken into account for the LAO/STO and LVO/STO, respectively. The thicknesses of the LAO and LVO adopted for the measurements are 11 uc.

attribution is validated by the above comprehensive analysis, and an electronically tuned WL-WAL transition is demonstrated for both the LAO/STO and LVO/STO.

When V_g further increases, the positive magnetoconductivity background turns to a negative one [26] [see Figs. 3(a) and 3(b)]. This negative background originates from B^2 magnetoresistivity primarily caused by the classical Lorentz force [27,32]. To better illustrate the WL/WAL quantum corrections, it is justifiable to subtract this classical background, as adopted previously for various WL/WAL systems [27,34–36].

The results are shown in Figs. 3(g) and 3(h). It is clear that B_{\min} increases initially and then drops as the V_g is swept from negative to positive. Since B_{\min} signifies the critical magnetic field where the WAL is overwhelmed mainly by the WL, its magnitude roughly reflects the SOC strength and has been shown to be proportional to the characteristic magnetic field for the SOC (B_{so}) [4,6,37]. Therefore the WAL results demonstrate unambiguously an unconventional Rashba SOC at the STO-based interfaces, whose magnitude can be tuned effectively to show a dome feature.

There are two widely used WL/WAL theoretical models developed by Hikami, Larkin, and Nagaoka (HLN) [38] and by Iordanskii, Lyanda-Geller, and Pikus (ILP) [39], respectively. The former is based on the Elliott-Yafet (EY) [40,41] spin-flip scattering mechanism and incorporates only the k -cubic SOC, whereas the latter is based on the Dyakonov-Perel (DP) [42] spin precession mechanism and takes both the k -linear and k -cubic SOC into account. Although the original WL/WAL theory considered only a single conduction band, it has been demonstrated that the single-band WL/WAL theory is also valid for multiband systems with an arbitrarily complex Fermi surface using the HLN model as an example, and the extracted characteristic parameters are averaged over the electronic states of all the bands around the Fermi level (E_F) [43]. Following this important development, the single-band WL/WAL picture has been successfully applied to many multiband systems [44–46]. Since the SOC in both the HLN and ILP models can be eventually characterized by the spin relaxation times quantitatively, the effective single-band picture should also be applicable for the ILP model. Moreover, when only the k -cubic SOC is present, the formula of the ILP model can be reduced to that of the HLN model [39,47]. Here we fitted the WAL results by adopting the ILP model (see more details in the Supplemental Material (SM) [48]), which allows us to make direct connections between the SOC and the band structures, since the SOC of different d subbands may possess different k dependence [9,10].

In order to determine the separated contributions from the linear and cubic Rashba effect, we fitted the WAL data using $r = B_{\text{so}1}/B_{\text{so}3}$ as a tuning parameter [6,27], where $B_{\text{so}1}$ ($B_{\text{so}3}$) is the characteristic field for k -linear (k -cubic) SOC. The fitting results for the LAO/STO at $V_g = -20$ V and LVO/STO at $V_g = 0$ V are shown in Figs. 3(e) and 3(f), and share the same features: When only the k -linear contribution ($r = \infty$) or both the k -linear and k -cubic contributions ($0 < r < \infty$) are taken into account, the fitting curves deviate from the experimental results substantially; on the other hand, excellent agreement is achieved when only the k -cubic contribution ($r = 0$) is considered. Furthermore, the k -cubic contribution also dominates from the fitting for all the adopted V_g s with WAL features, as shown in Figs. 3(g) and 3(h). Consequently, we conclude that only the k -cubic SOC is present at the LAO/STO and LVO/STO interfaces. The fitting parameter $B_{\text{so}3}$ will be denoted as B_{so} thereafter. The excellent fittings also suggest that other contributions, e.g., Coulomb interactions, are negligible.

Relying on the equivalence of the HLN and ILP models when only the k -cubic SOC is present, the HLN model has also been practically adopted to analyze the Rashba SOC in many two-dimensional systems [49,50], although the Rashba

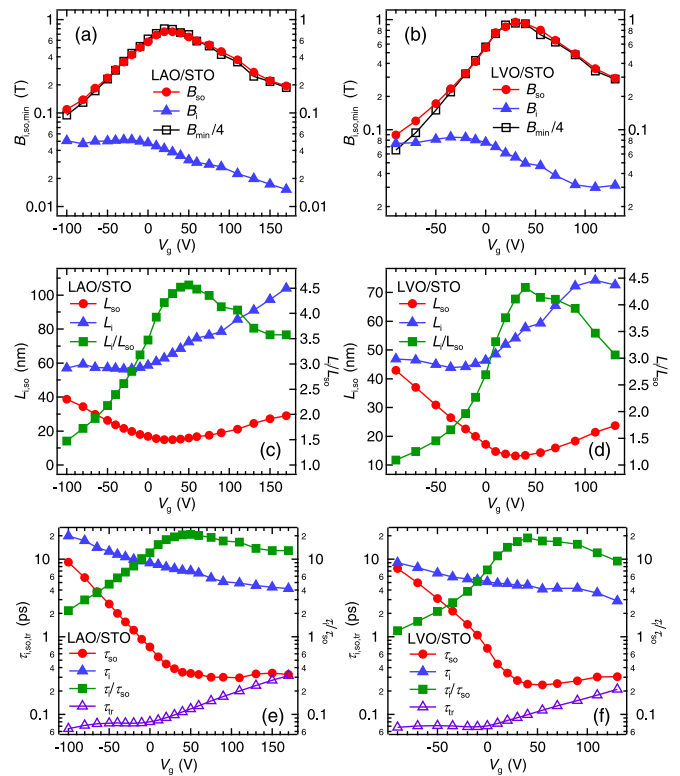


FIG. 4. (Color online) (a), (b) The inelastic scattering characteristic field B_i , the k -cubic SOC characteristic field B_{so} , and $B_{\min}/4$ as functions of V_g for the LAO/STO and LVO/STO, respectively. (c), (d) The phase coherence length L_i , the spin relaxation length L_{so} , and the ratio of L_i/L_{so} as functions of V_g for the LAO/STO and LVO/STO, respectively. (e), (f) The inelastic relaxation time τ_i , the spin relaxation time τ_{so} , and the ratio of τ_i/τ_{so} as functions of V_g for the LAO/STO and LVO/STO, respectively. The thicknesses of the LAO and LVO are 11 uc.

SOC is generally related to the DP spin precession mechanism. Here we also analyze the data using the HLN model [48], and the results reproduce that from the ILP fittings with $r = 0$.

The fitting parameters B_{so} and B_i (the characteristic field for inelastic scattering) are directly obtained from the fittings, as shown in Figs. 4(a) and 4(b). The phase coherence length (L_i) and spin relaxation length (L_{so}) are derived from the relation $L_{i,\text{so}} = \sqrt{\hbar/(4eB_{i,\text{so}})}$. In the effective single-band WL/WAL picture, it is justifiable to adopt an average effective mass m and use the total electron density n (the effective Fermi wave vector) to further derive other parameters [43,46]. The inelastic relaxation time (τ_i) and spin relaxation time (τ_{so}) are extracted from the relations $\tau_{i,\text{so}} = L_{i,\text{so}}^2/D$, $D = v_F^2 \tau_{\text{tr}}/2$, $v_F = \hbar k_F/m$, and $k_F = \sqrt{2\pi n}$, where D denotes the diffusion constant, τ_{tr} the transport scattering time, v_F the Fermi velocity, and k_F the Fermi wave vector. The m is assumed to be $1.5m_e$ [51] (m_e is the electron rest mass), and τ_{tr} is estimated from the Hall mobility, which increases monotonically with increasing V_g . The $B_{i,\text{so}}$, $\tau_{i,\text{so}}$, τ_i/τ_{so} , $L_{i,\text{so}}$, and L_i/L_{so} for the LAO/STO and LVO/STO interfaces as functions of V_g are plotted in Fig. 4. The obtained B_{so} is indeed proportional to B_{\min} with $B_{\text{so}} \sim B_{\min}/4$ [4,37]. The dependencies of B_{so} , L_{so} , L_i/L_{so} , τ_{so} , and τ_i/τ_{so} on V_g show nonmonotonic behaviors: The B_{so} ,

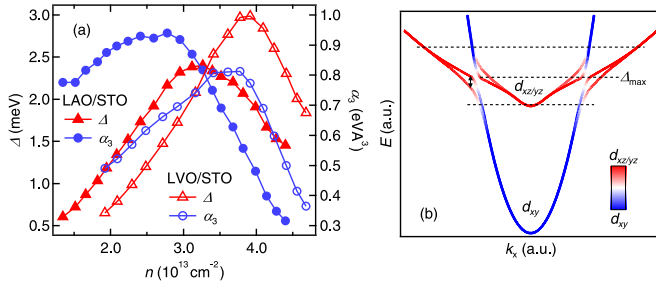


FIG. 5. (Color online) (a) The spin splitting Δ and k -cubic Rashba coefficient α_3 as functions of the electron density n for the 11-uc LAO/STO and 11-uc LVO/STO. (b) The band structure schematic of the STO-based interfaces only considering the lowest d_{xy} and $d_{xz/yz}$ subbands with SOC.

L_i/L_{so} , and τ_i/τ_{so} increase first and then drop with increasing V_g , while L_{so} and τ_{so} behave the other way around. Therefore the quantitative ILP fittings confirm that the SOC strength at both the LAO/STO and LVO/STO interfaces can be tuned by V_g to show a dome feature, consistent with the B_{min} behavior.

The spin splitting energy Δ and k -cubic Rashba coefficient α_3 can be eventually obtained from the relations $\Delta = \hbar\Omega_3 = \alpha_3 k_F^3$ and $\tau_{so}^{-1} = 2\Omega_3^2 \tau_{tr}$, where Ω_3 is the k -cubic Rashba term. The dependencies of Δ and α_3 on n are shown in Fig. 5(a) for both the LAO/STO and LVO/STO. As n increases, both Δ and α_3 first increase and then decrease after a critical n . The Δ peaks at $n = 3.3 \times 10^{13} \text{ cm}^{-2}$ ($V_g = 40 \text{ V}$) and $n = 3.9 \times 10^{13} \text{ cm}^{-2}$ ($V_g = 40 \text{ V}$) for the LAO and LVO, respectively. These values are close to the $n(V_g)$ signifying the apparent single- to two-carrier transition, suggesting strong connection between the two effects as will be discussed later.

Strictly speaking, the ILP theory is valid only in the diffusive regime ($B < B_{tr}$, where B_{tr} is the characteristic field for transport scattering). Here wider B intervals at high positive V_g s to include B_{min} are taken into account to achieve better fitting results, following Refs. [52] and [53]. On the other hand, we emphasize again that the nonmonotonic dependence of the SOC strength (B_{min} as a rough estimation) on the V_g is directly revealed [see Figs. 3(g) and 3(h) and Figs. 4(a) and 4(b)], irrespective of the fitting. It is also noted that m is assumed to be $1.5m_e$ to derive τ_{so} and Δ . This value is between the two effective masses ($0.9m_e$ and $2.0m_e$) estimated from multiband quantum oscillations [22], and reasonably reflects the average effective mass within a single-band picture of the present multiband systems. In addition, the effective mass of the $d_{xz/yz}$ subbands actually increases from the bottom with increasing E_F [8–12], leading to an increase of the average effective mass m . Nevertheless, the evolution in m does not change the nonmonotonic dependence of the SOC strength on n . According to the equations listed earlier, the increase of m only makes τ_{so} (Δ and α_3) rise (fall) more rapidly with n after reaching the minimum (maximum). Therefore from the above qualitative and quantitative analyses, we demonstrate that when V_g is varied, the SOC strength shows nonmonotonic dependence accompanied by an apparent single- to two-carrier transition. The two concomitant effects are independent on the overlayers (band insulator LAO or Mott insulator LVO). This observation further supports that the mobile carriers at the

interfaces primarily reside in the subbands derived from the Ti $3d$ orbitals, which is consistent with the electron reconstruction picture [14,24].

C. Nontrivial SOC mechanism

Next we discuss the mechanism leading to such nontrivial SOC at the STO-based interfaces. The standard Rashba mechanism dictates that the SOC strength is proportional to the interfacial electric field [4–6]. This simple picture however fails to explain the observed nonmonotonic dependence of SOC strength on V_g , since the interfacial electric field should change monotonically with the sweeping V_g for such single heterostructures. It is noted that for STO-based 2D electron systems, the conduction bands consist of multiple $3d$ subbands, and the bottom d_{xy} and $d_{xz/yz}$ subbands with different effective masses may cross each other [8–12]. Recently, the first-principles calculations and tight-binding analysis predicted that although relatively weak in both the d_{xy} and $d_{xz/yz}$ subbands, the SOC is substantially enhanced at the d_{xy} - $d_{xz/yz}$ crossing region [8–12], where the orbital mixing induces significant local orbital angular momentum [8]. This multiorbital effect can perfectly explain the observed dome feature in the band filling dependence of Δ and other physical parameters that rely on the SOC strength.

This mechanism is further supported by the observed apparent single- to two-carrier transition when V_g is swept as discussed earlier. This transition seems to indicate that the E_F crosses only the bottom d_{xy} subband at lower electron density and then is tuned to enter both the d_{xy} and $d_{xz/yz}$ subbands at higher electron density. However this picture is not valid: Tight-binding modeling found that the SOC is k linear for the d_{xy} subband and k cubic for the $d_{xz/yz}$ subbands due to the different symmetry of the d_{xy} and $d_{xz/yz}$ orbitals [9,10], while our experiments only reveal k -cubic SOC before and after the transition. Therefore the observed prevailing k -cubic SOC suggests that the $d_{xz/yz}$ electrons dominate the SOC effect and the contribution from the d_{xy} electrons is negligible.

On the other hand, theoretical studies revealed that the SOC will modify the band structure substantially to develop a tail with light mass at the bottom of the heavy $d_{xz/yz}$ subbands [8–12]. This provides a comprehensive scenario for both the apparent one- to two-carrier transition and nontrivial SOC behaviors, as depicted in Fig. 5(b): At low band filling, E_F crosses the d_{xy} subband and the light-mass tail of the $d_{xz/yz}$ subbands. Since the effective masses and mobilities of the d_{xy} subband and the tail of the $d_{xz/yz}$ subbands are both comparable, their combined Hall effect behaves as a single-carrier type as observed [12]. When E_F is lifted by tuning V_g , the mass of the $d_{xz/yz}$ subbands is getting heavy, and the two-carrier feature can now be distinguished. In accordance, the SOC mainly contributed from the $d_{xz/yz}$ electrons increases initially with increasing E_F , reaching maximum at the d_{xy} - $d_{xz/yz}$ crossing points, and then decrease with further increasing E_F . The above discussions are restricted to the V_g region where the WAL is observed. For relatively large negative V_g s without the WAL feature, E_F may cross solely the d_{xy} subband.

It is noted that the two critical V_g s (ns) signifying the single- to two-carrier transition and the SOC strength peak are close in value as revealed earlier, consistent with previous theoretical

prediction that the d_{xy} - $d_{xz/yz}$ crossings are close in energy to the light-heavy transition region in the $d_{xz/yz}$ subbands [12]. Besides, the previous controversial observations of the SOC strength dependent on V_g [25–27] can now be readily understood from the fact that they possess different electron density regions.

It is interesting to see that the domelike n dependence of the SOC strength almost resembles the dependence of the transition temperature of the superconductivity at the LAO/STO interfaces [12,29], suggesting that the superconductivity is unconventional and can be substantially manipulated by tuning the SOC strength [54]. Moreover, the demonstration of the SOC sensitive to the d -band structure for 2D d -electron systems may also open a door to explore oxide-based novel topologic phases [55,56]. On the other hand, the spin splittings for these STO-based electronic systems are comparable to that of conventional semiconductor electron systems, which also offer alternative platform to realize spintronic effects and devices, for example, the enhanced spin Hall effect due to the k -cubic SOC [57].

IV. CONCLUSION

In conclusion, we have established a direct relation between the unconventional Rashba SOC and the Ti $3d$ subband ordering for two STO-based 2D d -electron systems, i.e., LAO/STO and LVO/STO. The k -cubic Rashba effect originated from the $d_{xz/yz}$ states is revealed from the WAL

analysis. Moreover, when V_g is swept, the SOC strength initially increases and then decreases to form a dome feature. Meanwhile, an apparent single- to two-carrier transition in response to varying V_g is also discovered from the Hall measurement, evidencing ordering of the Ti $3d$ subbands. Such universal observations regardless of the boundary conditions strongly indicate that the nontrivial SOC is largely determined by the Ti $3d$ band structure, and the maximal spin splitting develops at the d_{xy} - $d_{xz/yz}$ crossing region as predicted, where the SOC is substantially enhanced by the band hybridization. The present findings offer new opportunities to explore oxide-based nontrivial quantum phases and spintronic devices.

ACKNOWLEDGMENTS

We thank Hua Wu, Jin Zhao, and Hua Zhou for helpful discussion and support. This work was supported in part by the National Natural Science Foundation of China (Grants No. 11434009, No. 11374279, No. 11461161009, No. 11304299, and No. 11174306), National Key Basic Research Program (Grant No. 2014CB921102), the Strategic Priority Research Program (B) of the Chinese Academy of Sciences (Grant No. XDB01020000), the Fundamental Research Funds for the Central Universities (Grant No. WK2340000011), and China Postdoctoral Science Foundation (Grant No. 2013M541829). Use of the Advanced Photon Source at Argonne National Laboratory was supported by the US Department of Energy, Office of Science, Office of Basic Energy Sciences, under Contract No. DE-AC02-06CH11357.

-
- [1] S. Datta and B. Das, *Appl. Phys. Lett.* **56**, 665 (1990).
 - [2] I. Žutić, J. Fabian, and S. Das Sarma, *Rev. Mod. Phys.* **76**, 323 (2004).
 - [3] R. Winkler, *Spin-Orbit Coupling Effects in Two-Dimensional Electron and Hole Systems* (Springer-Verlag, Berlin, 2003).
 - [4] G. L. Chen, J. Han, T. T. Huang, S. Datta, and D. B. Janes, *Phys. Rev. B* **47**, 4084 (1993).
 - [5] T. Koga, J. Nitta, T. Akazaki, and H. Takayanagi, *Phys. Rev. Lett.* **89**, 046801 (2002).
 - [6] R. Moriya, K. Sawano, Y. Hoshi, S. Masubuchi, Y. Shiraki, A. Wild, C. Neumann, G. Abstreiter, D. Bougeard, T. Koga, and T. Machida, *Phys. Rev. Lett.* **113**, 086601 (2014).
 - [7] A. F. Santander-Syro, O. Copie, T. Kondo, F. Fortuna, S. Pailhès, R. Weht, X. G. Qiu, F. Bertran, A. Nicolaou, A. Taleb-Ibrahimi, P. Le Fèvre, G. Herranz, M. Bibes, N. Reyren, Y. Apertet, P. Lecoeur, A. Barthélémy, and M. J. Rozenberg, *Nature (London)* **469**, 189 (2011).
 - [8] P. D. C. King, S. McKeown Walker, A. Tamai, A. de la Torre, T. Eknapakul, P. Buaphet, S.-K. Mo, W. Meevasana, M. S. Bahramy, and F. Baumberger, *Nat. Commun.* **5**, 3414 (2014).
 - [9] Z. Zhong, A. Tóth, and K. Held, *Phys. Rev. B* **87**, 161102 (2013).
 - [10] Y. Kim, R. M. Lutchyn, and C. Nayak, *Phys. Rev. B* **87**, 245121 (2013).
 - [11] G. Khalsa, B. Lee, and A. H. MacDonald, *Phys. Rev. B* **88**, 041302 (2013).
 - [12] A. Joshua, S. Pecker, J. Ruhman, E. Altman, and S. Ilani, *Nat. Commun.* **3**, 1129 (2012).
 - [13] A. Ohtomo and H. Y. Hwang, *Nature (London)* **427**, 423 (2004).
 - [14] N. Nakagawa, H. Y. Hwang, and D. A. Muller, *Nat. Mater.* **5**, 204 (2006).
 - [15] Z. S. Popović, S. Satpathy, and R. M. Martin, *Phys. Rev. Lett.* **101**, 256801 (2008).
 - [16] R. Pentcheva and W. E. Pickett, *Phys. Rev. Lett.* **102**, 107602 (2009).
 - [17] M. Sing, G. Berner, K. Goß, A. Müller, A. Ruff, A. Wetscherek, S. Thiel, J. Mannhart, S. A. Pauli, C. W. Schneider, P. R. Willmott, M. Gorgoi, F. Schäfers, and R. Claessen, *Phys. Rev. Lett.* **102**, 176805 (2009).
 - [18] H. X. Liang, L. Cheng, X. F. Zhai, N. Pan, H. L. Guo, J. Zhao, H. Zhang, L. Li, X. Q. Zhang, X. P. Wang, C. G. Zeng, Z. Y. Zhang, and J. G. Hou, *Sci. Rep.* **3**, 1975 (2013).
 - [19] M. P. Warusawithana, C. Richter, J. A. Mundy, P. Roy, J. Ludwig, S. Paetel, T. Heeg, A. A. Pawlicki, L. F. Kourkoutis, M. Zheng, M. Lee, B. Mulcahy, W. Zander, Y. Zhu, J. Schubert, J. N. Eckstein, D. A. Muller, C. Stephen Hellberg, J. Mannhart, and D. G. Schlom, *Nat. Commun.* **4**, 2351 (2013).
 - [20] G. Khalsa and A. H. MacDonald, *Phys. Rev. B* **86**, 125121 (2012).
 - [21] L. W. van Heeringen, G. A. de Wijs, A. McCollam, J. C. Maan, and A. Fasolino, *Phys. Rev. B* **88**, 205140 (2013).
 - [22] A. McCollam, S. Wenderich, M. K. Kruize, V. K. Guduru, H. J. A. Molegraaf, M. Huijben, G. Koster, D. H. A. Blank, G. Rijnders, A. Brinkman, H. Hilgenkamp, U. Zeitler, and J. C. Maan, *APL Mater.* **2**, 022102 (2014).

- [23] P. Perna, D. Maccariello, M. Radovic, U. Scotti di Uccio, I. Pallecchi, M. Codda, D. Marré, C. Cantoni, J. Gazquez, M. Varela, S. J. Pennycook, and F. Miletto Granozio, *Appl. Phys. Lett.* **97**, 152111 (2010).
- [24] Y. Hotta, T. Susaki, and H. Y. Hwang, *Phys. Rev. Lett.* **99**, 236805 (2007).
- [25] M. Ben Shalom, M. Sachs, D. Rakhmilevitch, A. Palevski, and Y. Dagan, *Phys. Rev. Lett.* **104**, 126802 (2010).
- [26] A. D. Caviglia, M. Gabay, S. Gariglio, N. Reyren, C. Cancellieri, and J.-M. Triscone, *Phys. Rev. Lett.* **104**, 126803 (2010).
- [27] H. Nakamura, T. Koga, and T. Kimura, *Phys. Rev. Lett.* **108**, 206601 (2012).
- [28] J. Biscaras, N. Bergeal, S. Hurand, C. Grossetête, A. Rastogi, R. C. Budhani, D. LeBoeuf, C. Proust, and J. Lesueur, *Phys. Rev. Lett.* **108**, 247004 (2012).
- [29] A. D. Caviglia, S. Gariglio, N. Reyren, D. Jaccard, T. Schneider, M. Gabay, S. Thiel, G. Hammerl, J. Mannhart, and J.-M. Triscone, *Nature (London)* **456**, 624 (2008).
- [30] G. Bergmann, *Phys. Rep.* **107**, 1 (1984).
- [31] M. Kohda, T. Bergsten, and J. Nitta, *J. Phys. Soc. Jpn.* **77**, 031008 (2008).
- [32] N. W. Ashcroft and N. D. Mermin, *Solid State Physics* (Saunders, New York, 1976).
- [33] V. K. Guduru, A. McCollam, A. Jost, S. Wenderich, H. Hilgenkamp, J. C. Maan, A. Brinkman, and U. Zeitler, *Phys. Rev. B* **88**, 241301 (2013).
- [34] R. L. Kallaher, J. J. Heremans, N. Goel, S. J. Chung, and M. B. Santos, *Phys. Rev. B* **81**, 075303 (2010).
- [35] D. Lükermann, S. Sologub, H. Pfnür, C. Klein, M. Horn-von Hoegen, and C. Tegenkamp, *Phys. Rev. B* **86**, 195432 (2012).
- [36] Y. Zhang, R. L. Kallaher, V. Soghomonian, and J. J. Heremans, *Phys. Rev. B* **87**, 054430 (2013).
- [37] P. D. Dresselhaus, C. M. A. Papavassiliou, R. G. Wheeler, and R. N. Sacks, *Phys. Rev. Lett.* **68**, 106 (1992).
- [38] S. Hikami, A. Larkin, and Y. Nagaoka, *Prog. Theor. Phys.* **63**, 707 (1980).
- [39] S. V. Iordanskii, Yu. B. Lyanda-Geller, and G. E. Pikus, *JETP Lett.* **60**, 206 (1994).
- [40] R. J. Elliott, *Phys. Rev.* **96**, 266 (1954).
- [41] Y. Yafet, *Solid State Phys.* **14**, 1 (1963).
- [42] M. I. Dyakonov and V. I. Perel, *Sov. Phys. Solid State* **13**, 3023 (1972).
- [43] D. Rainer and G. Bergmann, *Phys. Rev. B* **32**, 3522 (1985).
- [44] B. J. Hickey, D. Greig, and M. A. Howson, *Phys. Rev. B* **36**, 3074 (1987).
- [45] E. I. Buchstab, A. V. Butenko, N. Ya. Fogel, V. G. Cherkasova, and R. L. Rosenbaum, *Phys. Rev. B* **50**, 10063 (1994).
- [46] D. Stornaiuolo, S. Gariglio, A. Fête, M. Gabay, D. Li, D. Massarotti, and J.-M. Triscone, *Phys. Rev. B* **90**, 235426 (2014).
- [47] W. Knap, C. Skierbiszewski, A. Zduniak, E. Litwin-Staszewska, D. Bertho, F. Kobbi, J. L. Robert, G. E. Pikus, F. G. Pikus, S. V. Iordanskii, V. Mosser, K. Zekentes, and Yu. B. Lyanda-Geller, *Phys. Rev. B* **53**, 3912 (1996).
- [48] See Supplemental Material at <http://link.aps.org/supplemental/10.1103/PhysRevB.92.075309> for details of the WL/WAL model.
- [49] S. Knott, T. Ch. Hirschmann, U. Wurstbauer, W. Hansen, and W. Wegscheider, *Phys. Rev. B* **84**, 205302 (2011).
- [50] N. Miyata, H. Narita, M. Ogawa, A. Harasawa, R. Hobara, T. Hirahara, P. Moras, D. Topwal, C. Carbone, S. Hasegawa, and I. Matsuda, *Phys. Rev. B* **83**, 195305 (2011).
- [51] A. D. Caviglia, S. Gariglio, C. Cancellieri, B. Sacépé, A. Fête, N. Reyren, M. Gabay, A. F. Morpurgo, and J.-M. Triscone, *Phys. Rev. Lett.* **105**, 236802 (2010).
- [52] B. Grbić, R. Leturcq, T. Ihn, K. Ensslin, D. Reuter, and A. D. Wieck, *Phys. Rev. B* **77**, 125312 (2008).
- [53] H. Nakamura and T. Kimura, *Phys. Rev. B* **80**, 121308 (2009).
- [54] K. Michaeli, A. C. Potter, and P. A. Lee, *Phys. Rev. Lett.* **108**, 117003 (2012).
- [55] A. Rüegg and G. A. Fiete, *Phys. Rev. B* **84**, 201103 (2011).
- [56] D. Xiao, W. Zhu, Y. Ran, N. Nagaosa, and S. Okamoto, *Nat. Commun.* **2**, 596 (2011).
- [57] J. Schliemann and D. Loss, *Phys. Rev. B* **71**, 085308 (2005).